Turbulence modelling analysis in a corner separation flow

Jean-François Monier, Feng Gao, Jérôme Boudet, L. Shao

Turbulence modelling analysis in a corner separation flow

Jean-François Monier[a,b,*], Feng Gao[c], Jérôme Boudet[b], Liang Shao[b]

[a] *Safran Aircraft Engines, Rond-point René Ravaud, 77550 Moissy-Cramayel, France*
[b] *LMFA, UMR CNRS 5509, Univ Lyon, École Centrale de Lyon, Écully cedex, F-69134, France*
[c] *Research Institute of Aero-Engine, Beihang University, Beijing 102206, P.R. China*

Abstract

This paper studies RANS turbulence modelling for a linear compressor cascade corner separation flow, using large-eddy simulation results as reference. The Boussinesq and the quadratic constitutive relations are investigated with two versions of Wilcox's $k-\omega$ turbulence model through a priori and a posteriori analyses. In the a priori analysis the quadratic constitutive relation shows improvement on the alignment between the rate-of-strain tensor and the Reynolds stress tensor for the inlet region, compared to the Boussinesq constitutive relation. But the improvement is less significant in the highly vortical region. Using the turbulent kinetic energy and the specific dissipation rate provides a fairly good estimate of the turbulent viscosity. The turbulent kinetic energy budget is also investigated. Large-eddy simulation results present non-equilibrium turbulence, *i.e.* the production and dissipation are not balanced, whereas the RANS models predicts equilibrium turbulence.

Keywords: large-eddy simulation, Reynolds-averaged Navier-Stokes, turbulence modelling, constitutive relation, turbulent kinetic energy budget, corner separation

2018 MSC: 00-01, 99-00

*Corresponding author
Email address: jean-francois.monier@ec-lyon.fr (Jean-François Monier)

1. Introduction

The world aircraft fleet is expected to double within the next thirty years[1]. The resulting traffic increase will lead to economical and environmental challenges. The operation costs of jet engines have to be reduced. One strategy to reduce the operation costs and emissions of turbojet engines lies in the control of the secondary flows that develop within the compressor blade passages. These three-dimensional highly-vortical flows limit the blade loading and the efficiency, and affect the stability of the compressor. The control of these flows requires a fine understanding of their physics and the ability to accurately simulate their behaviour.

Corner separation is one of these secondary flows. It occurs where two orthogonal boundary-layers interact. For a compressor, it occurs at the junction of the end-wall (hub or casing) and the blade suction side. The presence of a strong pressure gradient in the compressor further complicates its behaviour. Extensive efforts has been devoted to compressor corner separation through experiment [2, 3, 4, 5, 6, 7] and numerical simulations [8], but its physics is neither entirely understood nor mastered.

Computational fluid dynamics (CFD) is essential in modern turbomachinery development. Reynolds-averaged Navier-Stokes (RANS) is the most common type of methods used in industry. RANS provides a 3D viscous description of the averaged flow, where the effects of turbulence are modelled, and its computational cost is affordable in a design cycle. However, it tends to over-predict the size and intensity of the corner separation[9, 10, 11]. Bordji *et al.*[12] reported that the quadratic constitutive relation (QCR) [13] yielded better results, for external aerodynamics. Regarding internal flows, Su and Yuan [14] report an improvement on the simulation of corner separation with the QCR. Both Bordji *et al.* and Su and Yuan applied the QCR to the Spalart-Allmaras turbulence model [15]. Beside RANS, large-eddy simulation (LES) is a different approach that relies on a direct description of the large turbulent eddies[16]. It can simulate highly vortical flows [17, 18], including corner separation[19, 11, 20], better

than RANS simulations but at a much greater computational cost.

In the present paper the turbulence characteristics, including Reynolds stresses and turbulent kinetic energy (TKE) budget, are analysed on a plane downstream of a corner separation, using LES[11], and compared with RANS results. Beforehand, the extraction of the TKE budget for LES is validated on a flat-plate boundary-layer test case against a direct numerical simulation (DNS) by Jiménez *et al.*[21]. The Boussinesq hypothesis, underlying many common RANS approaches, along with the QCR, are analysed using LES as reference.

2. Test-case and solver

The corner separation test-case represents a passage of a NACA65 linear compressor cascade experimentaly studied by Ma[22] (see also [23, 7]) and Zambonini[24] (see also [25, 26]).

The corner separation case has been numerically studied by Gao[19] (see also [11, 20, 27]). The LES simulation (in ref [19]) is used as a reference database for the present work.

All simulations have been carried out with *Turb'Flow*, an in-house compressible solver that allows LES and RANS simulations. Readers are referred to ref. [28] for further information about *Turb'Flow*.

2.1. Geometry and dimensions of the computational domain

The experimental compressor cascade is composed of 13 identical NACA 65-009 blades, whose camber angle has been modified to 23.22°. The original geometry and the modifications can be found in the theses of Zambonini[26] and Gao[19]. The blade chord length is $c = 150$mm, the stagger angle $\gamma = 42.7°$, the pitch length $s = 134.0$mm and the span length $h = 370.0$mm. The passage is simulated up to one and a half chord length upstream of the blade leading edge and two chord length downstream of the blade trailing edge. In order to restrain the computational cost in LES, only a half of the channel span was simulated ($h/2 = 185.0$mm), with a symmetry condition. The same half channel

is simulated in RANS, in order to be comparable. The stream-wise direction is denoted x_1, the pitch-wise direction x_2 and the span-wise direction x_3, as shown in figure 1.

2.2. Flow characteristics

The free-stream velocity is set to the same value as for the experiment, *i.e.* $u_e = 40\text{m.s}^{-1}$. It yields a Mach number $M \approx 0.12$, and the flow can be considered as incompressible. The reference density is $\rho_e = 1.177\text{kg.m}^{-3}$, and the dynamic viscosity is $\mu = 1.81 \times 10^{-5}\text{kg.m}^{-1}\text{s}^{-1}$, yielding a chord based Reynolds number $\text{Re}_c = 3.82 \times 10^5$. All simulations are carried out at the incidence angle 4°.

2.3. Mesh

Two different meshes are considered, a wall-resolved LES mesh and a RANS mesh.

The LES uses an HOH blade-to-blade mesh duplicated 481 times along the span-wise direction. A 2D representation (blade-to-blade plane) of the mesh (truncated upstream and downstream) is shown in figure 1. The cell dimensions at the walls (blade and end-wall) satisfy: less than 60 in the flow direction, $\Delta y^+ \leqslant 2$ in the wall-normal direction on the blades and the end-wall, and less than 30 in the cross-flow direction near the blade and the end-wall. The *a posteriori* calculated Δy^+ values on the blade and the end-wall are shown in figure 2. This allows resolving of the main turbulent structures near the walls. The tripping bands used to force the laminar/turbulent transition in the experiment (3.0mm wide by 0.3mm thick, located at 6.0mm from the leading edge, more details in [22]) are reproduced in the LES by steps (removal of some grid points) at the same locations. The total grid point number is about 2×10^8.

The RANS uses a similar but coarser mesh as used in the LES. The 2D blade-to-blade mesh is duplicated 77 times along the span-wise direction. The refinement is chosen to yield a wall-normal cell size $\Delta y^+ \leqslant 2$ [19]. The values of Δy^+ on the blade and the end-wall are given in figure 2. The RANS simulations

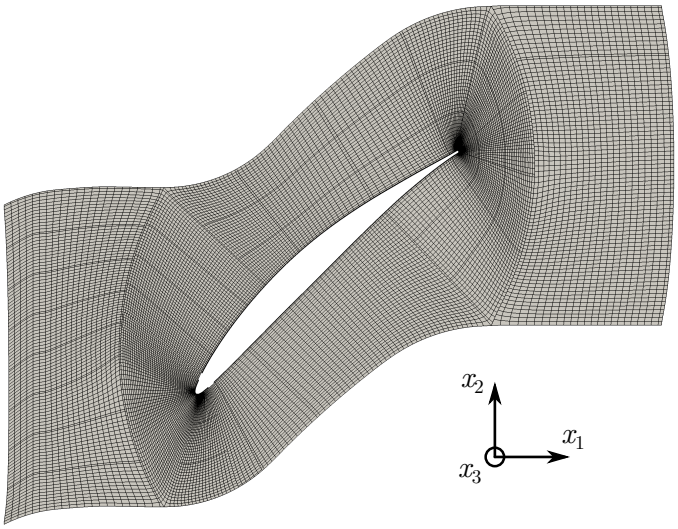

Figure 1: LES mesh around the blade. Every fourth point in each direction is plotted.

are fully turbulent, and the tripping bands are discarded. The total number of points is about 2.8×10^6, which is consistent with other RANS studies on corner separation [14].

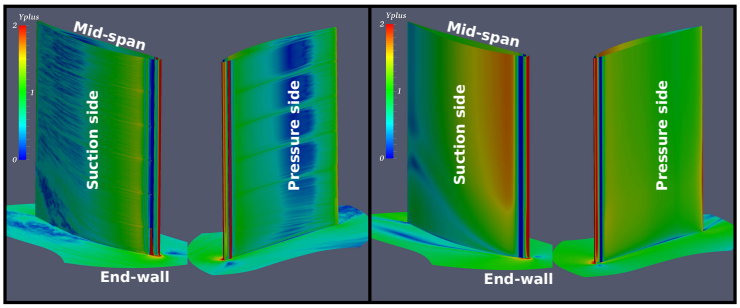

LES RANS Original k-ω

Figure 2: Δy^+ on the blade and the end-wall surfaces for LES and RANS, extracted from Gao [19].

2.4. Boundary conditions

Generating a turbulent inflow for LES is a burning issue. In order to provide a physically-sound turbulent boundary layer to the LES, a flat-plate boundary

layer simulation using three-dimensional, wall resolved LES is realised in parallel with the passage simulation. The instantaneous density and velocity vector are extracted on a plane from this simulation at the location where the time-averaged displacement thickness equals the experimental value at the inlet of the blade passage. The flat-plate simulation has a limited pitch-wise extension ($\sim \delta$, with δ the boundary-layer thickness at the blade passage inlet) which is repeated periodically to feed the blade passage inlet. In the free-stream region, due to the weak intensity of turbulence, the quantities are averaged in space and imposed at the inlet plane of the blade passage. This ensures consistent inflow conditions between the LES and the experiment. An illustration of the inflow generation is given in figure 3. The flat-plate domain is $\sim 76\delta$ long, its width is $1/4s$ ($\sim \delta$) and its height is $\sim 2\delta$. The total number of points in the flat-plate domain is around 1×10^8. The turbulent transition for the flat plate is triggered by a tripping band represented by a step in the grid. The band is located at $\mathrm{Re}_x = 1.3 \times 10^6$, and measures 4.8mm long by 0.673mm thick, and it is modelled by removing cells from the smooth mesh.

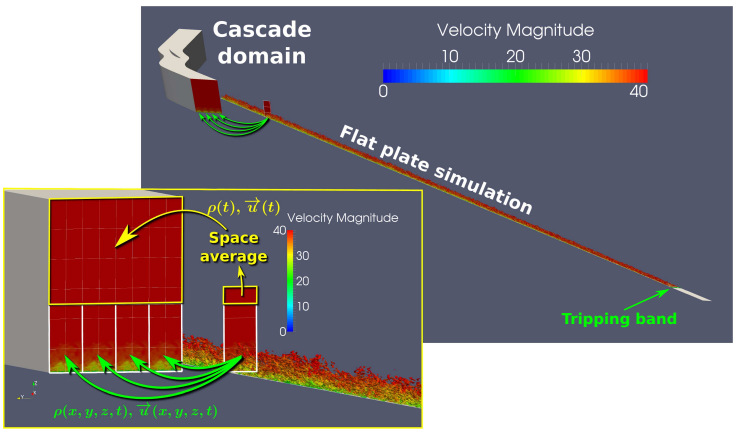

Figure 3: Corner separation inflow configuration, from Gao[19].

For the inflow of the RANS simulations, a two dimensional steady RANS simulation of a flat-plate boundary-layer is carried out. As for the LES, profiles are extracted at the location where the displacement thickness matches the

experimental value. The density, the three components of velocity, and the two turbulent variables are imposed as inlet profiles.

The pitch-wise boundary condition is set to periodic for all simulations. The boundary condition at mid-span is set as symmetric, in all simulations. All walls are set as no-slip adiabatic.

The outlet boundary condition is set to a partially non-reflective pressure condition for all simulations. In LES, a particular attention has been paid to the correct evacuation of the numerical acoustic waves at the outlet. In order to damp the unwanted numerical reflections, the mesh is stretched in the stream-wise direction and an explicit filter[29] is implemented for the last 20 grid planes (whose normals are in the stream-wise direction). The filter is also used near the blade leading and trailing edges over five grid points in the whole span, in order to smooth the oscillations present close to stagnation points.

2.5. Numerical schemes

The spatial scheme used for the inviscid fluxes is a four-point centred scheme from Jameson[30], with a fourth-order artificial viscosity (coefficient: 0.002 for the LES, 0.02 for the RANS simulations, see [31] for its definition). The spatial scheme for the viscous fluxes is a two-point centred scheme for all simulations.

For the LES, the temporal scheme is a three-step Runge-Kutta scheme with a constant time step of 2.5×10^{-8}s, yielding a Courant-Friedrichs-Lewy (CFL) number of 0.95 based on the minimum grid size 1.0×10^{-5}m, the reference velocity 40 m.s^{-1} and the speed of sound 340 m.s^{-1}. For RANS simulations, a five-step Runge-Kutta scheme is used for the time discretisation with a local variable time step at a CFL number 0.7 (based on local grid size, local velocity and local speed of sound). Given that the simulations are realised at a low Mach number, a low-Mach preconditioning [32] is applied for all RANS simulations.

2.6. Subgrid-scale/Turbulence models

The SISM subgrid-scale (SGS) model [33] is used in the LES. The characteristic frequency of the exponential averaging used in the model is calculated based on the free-stream velocity u_e and the chord length c, as $2u_e/c = 533$Hz.

For RANS simulations, three turbulence models are used: the original Wilcox $k-\omega$ turbulence model [34] (referenced as 'original $k-\omega$' thereafter), the quadratic Wilcox $k-\omega$ turbulence model [13][1] ('QCR $k-\omega$'), and the modified Wilcox $k-\omega$ turbulence model[10] ('modified $k-\omega$').

In the modified $k-\omega$ turbulence model, the production of ω is multiplied by a factor fr_1 defined as follows:

$$fr_1 = -\frac{1}{2\pi}\arctan\left(5\left(\frac{\Omega}{S}-1.2\right)\right)+0.75 \tag{1}$$

with S being the modulus of the mean strain-rate tensor and Ω the modulus of the mean rotation tensor.

2.7. Grid independence

In order to assess the grid independence of the RANS simulations, a finer mesh has been tested for the original $k-\omega$ simulation. For this new mesh, referenced to as the 'refined mesh', the number of grid points is doubled in each direction, compared to the original mesh. The total number of points of the refined mesh is about 16×10^6 points. The wall-normal cell size is halved ($y^+ \leqslant 1$, and $y^+ \leqslant 0.4$ in the corner separation area) compared to the original mesh.

The grid convergence is assessed for the mean pressure coefficient (whose formulation is given in equation (2) around the blade. Figure 4 plots the blade mean pressure coefficient from mid-span to near the end-wall. The span-wise locations where the mean pressure coefficient is extracted are presented thereafter, in figure 8.

For all the span-wise positions, the pressure coefficient show very little difference between the simulations with the original mesh and the refined mesh. The original mesh is sufficiently refined to yield the correct physics. From this point on, all the results presented are based on the original mesh.

[1] The QCR is originally presented for the Spalart-Allmaras turbulence model. In the present case, it has been adapted to the the Wilcox $k-\omega$ turbulence model.

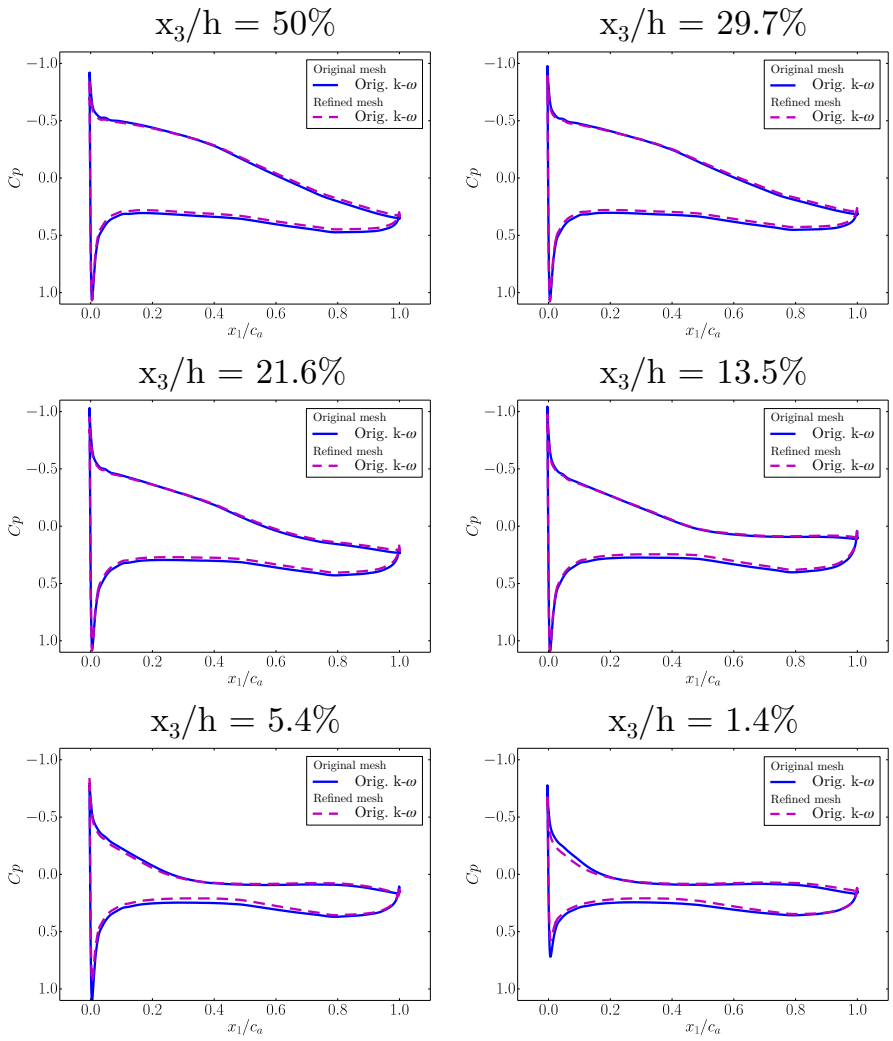

Figure 4: Mean static pressure coefficient around the blade at various span-wise positions.

2.8. Statistics

For LES, which is naturally unsteady, the transient regime at the beginning of the computation corresponds to the phase of numerical convergence. Additional ten flow-through periods (defined as the ratio between the chord length c and the free-stream velocity u_e) have been simulated to collect statistics, after the transient regime. These generates during 40.25ms, with one sample every

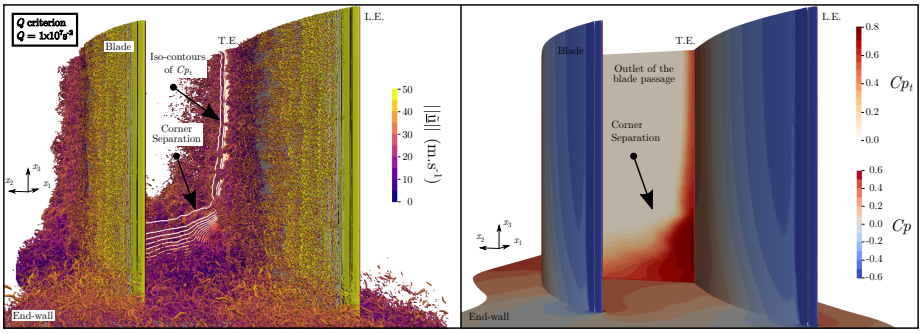

Figure 5: Visualisation of the LES flow field. Left: instantaneous Q criterion iso-surface ($Q = 1 \times 10^7 \mathrm{s}^{-2}$). Right: Mean pressure coefficient on the blade and the end-wall, and mean total pressure coefficient at the outlet of the blade passage. The same scale and colourmap are used for Cp_t in both figures.

50μs (2000 iterations), 805 samples.

For the RANS simulations, convergence is assessed by the residuals. The mean values of the conservative variables are directly provided by the steady solution.

3. Mean flow results

This section presents the mean flow characteristics. Prior to this, a visualisation of the corner separation (using Q-criterion and pressure coefficients) is presented in figure 5 with the LES solution.

First, the flow is visualised through limiting streamlines over the blade and endwall surfaces. Some results on the mean values, such as the static pressure coefficient around the blade or the total pressure losses, are presented to evaluate the overall performance of the LES and RANS simulations. Then, the Reynolds stresses are analysed on a plane downstream of the blade trailing edge.

Another more detailed characterisation of the LES can be found in ref.[11], with, for instance, the ratio of the SGS dissipation to the total dissipation (lying between 0.0 and 0.85 for the entire domain).

3.1. Limiting streamlines

The limiting streamlines over the blade suction side surface and the passage endwall are presented in figure 6 for all the simulations. These indicate the extent of the corner separation over the blade surface. For the LES, the separation occurs around mid-chord, and covers around one third of the half-span presented here. Compared to the LES, all RANS simulations over-estimate the corner separation. The separation occurs further upstream, and covers about one half of the half-span presented. The simulation with the original $k-\omega$ model predicts the largest corner separation region. The modified $k-\omega$ model gives a slightly reduced corner separation compared to the original $k-\omega$ but still larger than the LES. The QCR $k-\omega$ model gives a better estimation of the node-saddle (NS) point position, but the extent of the corner separation is over-predicted over the span. The focus points predicted by the QCR $k-\omega$ model are slightly upstream of those predicted by the original $k-\omega$ one. The position the end-wall focus point indicates that the corner separation in the QCR $k-\omega$ is smaller than in the other RANS simulations. A direct comparison of the topologies by all simulations is given in figure 7.

3.2. Static and total pressure coefficient

In order to gauge the performance of the simulations, the mean static and total pressure coefficients calculated with the LES and RANS solutions are compared with the experimental results [22]. The mean static pressure coefficient is defined as:

$$Cp = \frac{p - p_e}{0.5\rho_e u_e^2} \tag{2}$$

with p the local mean static pressure, p_e the inflow mean static pressure, ρ_e the inflow freestream density and u_e the inflow freestream velocity. The mean total pressure loss coefficient is defined as:

$$Cp_t = \frac{p_{te} - p_t}{p_{te} - p_e} \tag{3}$$

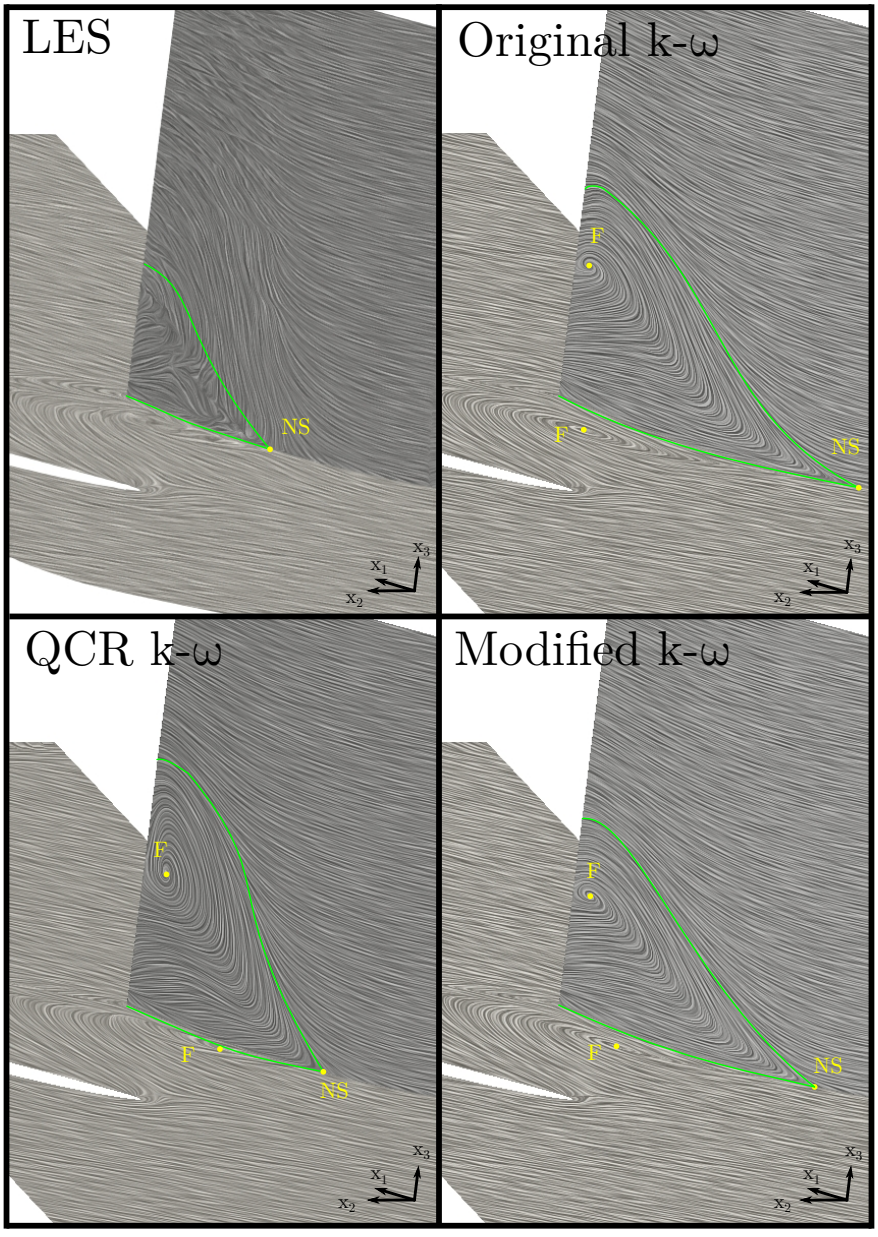

Figure 6: Limiting streamlines of the mean flow for the LES and the RANS simulations. For the RANS simulations, focus points (F) of the blade and the endwall are shown. For each simulation, the node-saddle (N-S) point at the junction of the blade and the end-wall, where the corner separation begins, is marked. The green line represents the edge of the separation on the blade suction side.

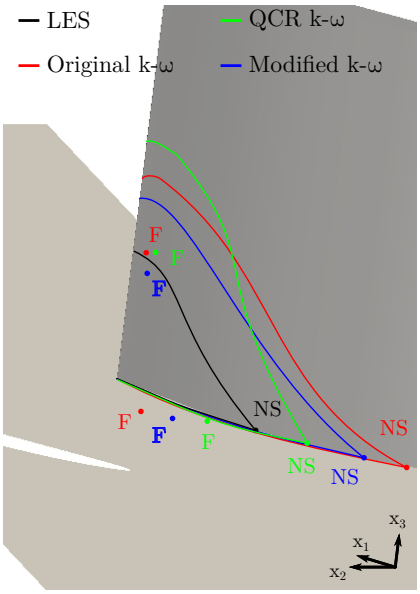

Figure 7: Comparison of the size of the corner separations. 'F' indicates the focus points. 'N-S' represents the node-saddle points at the junction of the blade and the end-wall, where the corner separation begins.

with p_{te} the mean inflow total pressure, p_t the local mean total pressure. The static pressure coefficient is extracted around the blade at six span-wise positions. The total pressure loss coefficient is extracted on the 'outlet 1' plane downstream of the blade passage outlet. These are shown in figure 8.

The mean static pressure coefficient Cp is presented in figure 9. Some oscillations are present close to the leading edge in the LES simulation due to the tripping bands. The upper branch of the curves represents the suction side, while the lower branch corresponds to the pressure side.

At mid-span and at 29.7% span, a fairly good agreement is achieved between the experiment and all simulations where the flow is attached to the blade. At 21.6% span a fairly good agreement can still be observed between the experiment, the LES, the quadratic and the modified $k-\omega$ models. The original $k-\omega$ model shows some difference with the others solutions, presenting a slight flattening of the pressure distribution on the suction side for $x_1/c_a \geqslant 0.75$. This

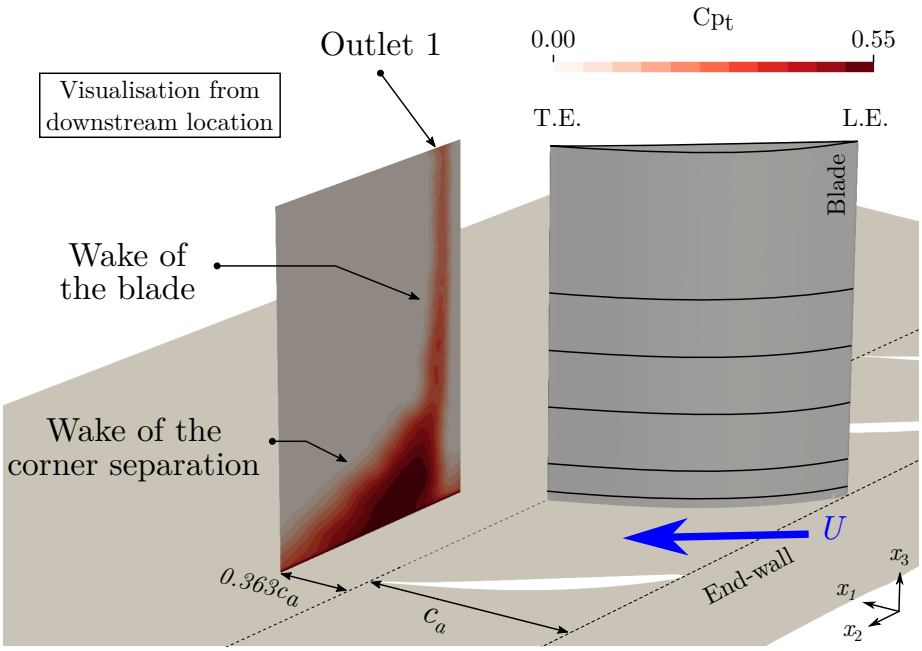

Figure 8: Extraction locations for Cp and Cp_t. The static pressure coefficient is extracted on the blade surface at six span-wise positions, indicated with black lines. The total pressure coefficient is exctracted on the plane 'outlet 1'. The axis origin is located at the junction between the blade leading edge and the end-wall.

plateau, related to boundary layer separation, occurs for all the simulations close to the end-wall as the corner separation develops. The QCR $k-\omega$ model presents less pressure drop than the original $k-\omega$ model, indicating weaker separation intensity near the blade trailing edge. Close to the end-wall, the QCR $k-\omega$ model shows the best performance among the RANS models. The modified $k-\omega$ model solution becomes less consistent with the experiment and the LES, but performs better than the original $k-\omega$ model.

A sudden and important static pressure drop is visible at the trailing edge. This is a known feature of steady simulations, reported by Denton[35] as the difficulty to capture the separation at the trailing edge.

The total pressure loss coefficients on the plane 'outlet 1' are shown in figure 10. The experimental and LES total pressure losses are very similar, differ-

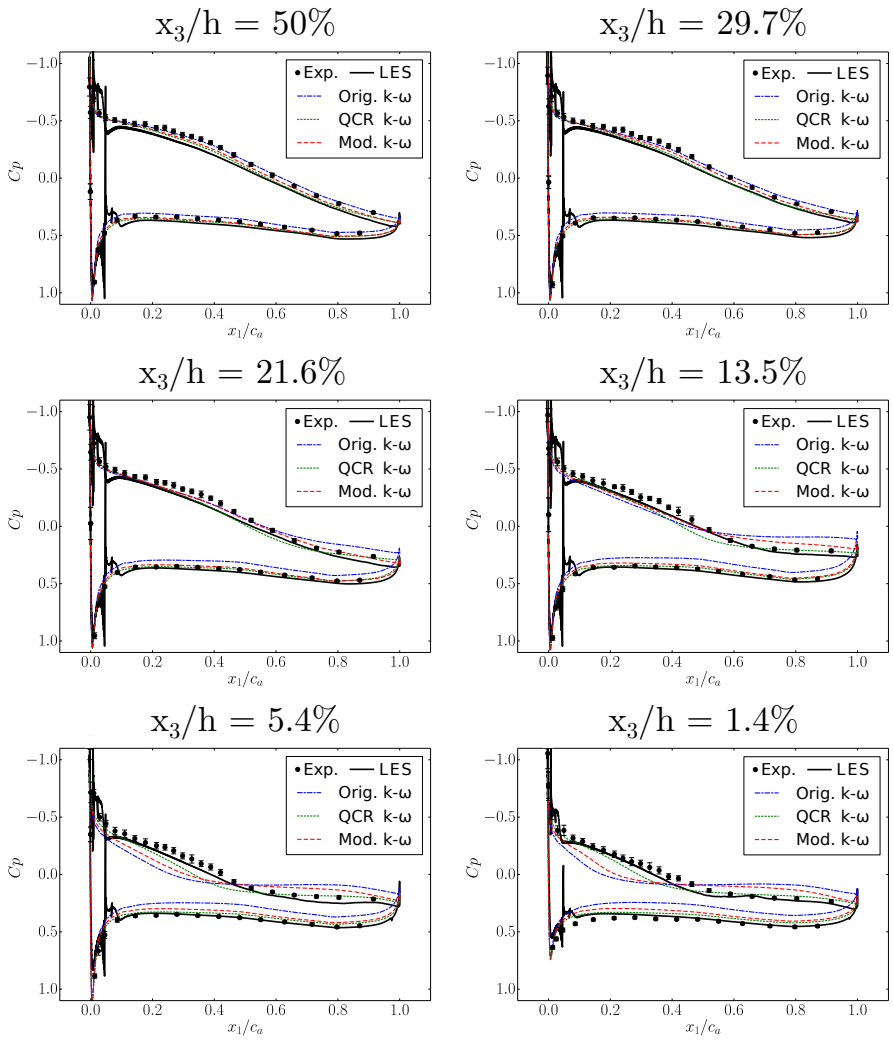

Figure 9: Mean static pressure coefficient around the blade at various span-wise positions. The vertical bars on the experimental results indicate the measurement uncertainties.

ing significantly from the RANS results. Therefore, the LES data are used as a reference for further detailed analysis, in order to understand why RANS generally fails in predicting this kind of flows. All RANS simulations over-predict the losses. Among the RANS models the QCR $k-\omega$ model achieves the closest agreement with the experiment and the LES. The modified Wilcox model

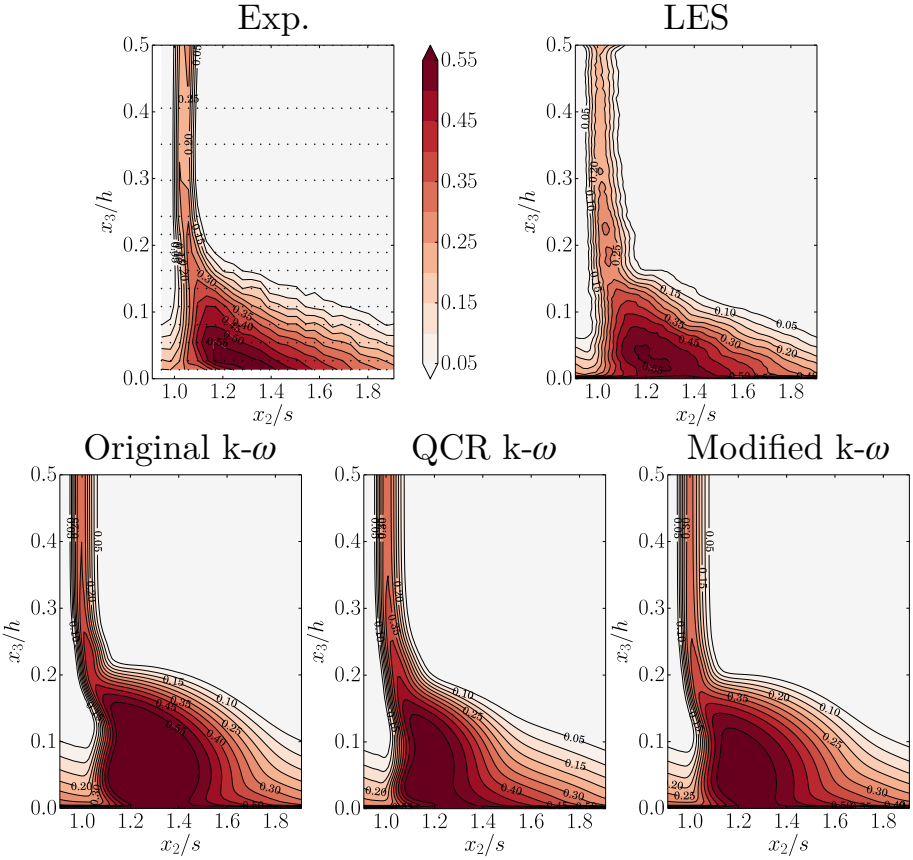

Figure 10: Mean total pressure loss coefficient on plane 'outlet 1'.

improves the intensity of the losses compared to the original Wilcox model, but not the size or the shape of the loss region. The corner separation wake remains too wide and too curved compared with the experimental or LES results.

3.3. Reynolds stresses

The RANS turbulence models affect the Navier-Stokes equations through the Reynolds stresses. Their accurate description is important for reliable and accurate simulations. The Reynolds stresses are defined as :

$$\forall (i,j) \in [\![1 \ ; \ 3]\!]^2, \tau_{tij} = -\left\langle \rho u_i'' u_j'' \right\rangle \tag{4}$$

with $\underline{u}''$ the fluctuation of the velocity $\underline{u}$ and ρ its local density. The Reynolds stresses are modelled in the RANS simulations via the Boussinesq constitutive relation (for the original and modified $k-\omega$ simulations) presented in eq. (5), and the QCR presented in eq. (6). All the constitutive relations use a turbulent viscosity, denoted μ_t, calculated as $\mu_t = \langle\rho\rangle\,[k]\,/\,[\omega]$.

Note that for a given quantity φ, the ensemble average is denoted $\langle\varphi\rangle$ and the fluctuating part is denoted φ', with the relation $\varphi = \langle\varphi\rangle + \varphi'$. Because the compressible Navier-Stokes equations are considered, the Favre average[36] is used. Considering ρ the density, the Favre average is denoted $[\varphi] = \langle\rho\varphi\rangle\,/\,\langle\rho\rangle$, and the Favre fluctuating part is denoted[2] φ'', with the relation $\varphi = [\varphi] + \varphi''$.

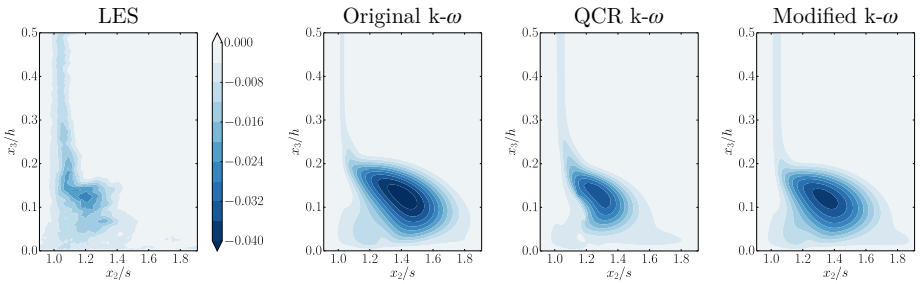

Figure 11: τ_{t11} on the plane 'outlet 1', normalised by $\rho_e u_e^2$.

The normal Reynolds stresses τ_{t11} at the section 'outlet 1' are shown in figure 11. Two zones are visible on the LES results: the wake of the blade boundary-layer ($x_2/s \in [1.0, 1.1]$, $x_3/h \in [0.2, 0.5]$) and the wake of the corner separation ($x_2/s \in [0.9, 1.5]$, $x_3/h \in [0.0, 0.2]$).

In the wake of the corner separation, the RANS simulations mis-predict the intensity of the LES normal Reynolds stress τ_{t11}. The RANS loss areas are also wider and farther from the blade boundary layer wake than the LES. A clear improvement is achieved with the QCR, by reducing the intensity and the loss area. The modified Wilcox model yields similar results to the original Wilcox

[2]Note that the same notation φ' is used for the ensemble-averaged fluctuating part and the large-scale filtered fluctuating part. Moreover, the same notation φ'' is used for the Favre averaged fluctuating part and the Favre filtered fluctuating part.

model, but with slightly reduced intensity. However, the improvement is not sufficient to get close to the LES results.

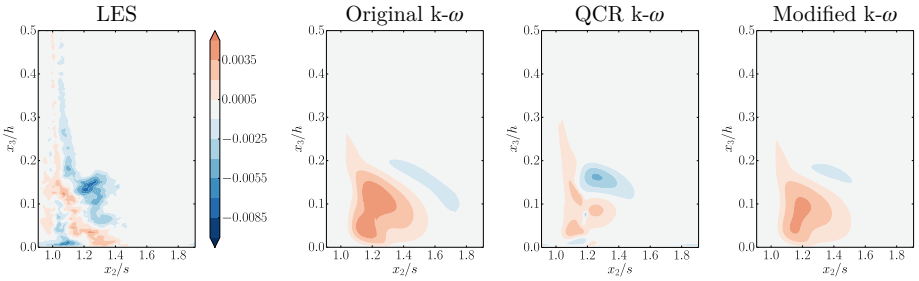

Figure 12: τ_{t12} on the plane 'outlet 1', normalised by $\rho_e u_e^2$.

The shear Reynolds stresses τ_{t12} on the 'outlet 1' plane are given in figure 12. The strong stress areas in the LES results are the same as for the normal Reynolds stresses.

The blade wake intensity is under-predicted by RANS for $x_3/h \geqslant 0.3$, compared to the LES. The RANS simulations mis-predict again the size and the intensity of the Reynolds stress τ_{t12}, downstream of the separation region. Contrary to the tendency for the normal stresses, the original and the modified $k-\omega$ models under-predict the intensity of negative stress values and over-predict positive stress values. The QCR $k-\omega$ model tends to correct this behaviour, and presents again the best agreement with the LES, in terms of both topology and intensity.

The differences between the LES and RANS Reynolds stresses remain significant. In order to explain this mismatch, the RANS turbulence modelling is investigated in two steps. First, the hypotheses of alignment and proportionality for both the Boussinesq and the QCR formulations are analysed. Then, the TKE budget modelled in the RANS is compared to that resolved by the LES.

4. Constitutive relation analysis

4.1. Alignment criterion and turbulent viscosities

Constitutive relations

The Boussinesq constitutive relation, used in both the original and modified $k-\omega$ models, assumes the Reynolds stress tensor satisfies:

$$\underline{\underline{\tau}}_t + \frac{2}{3}\langle\rho\rangle[k]\,\underline{\underline{I_3}} = \mu_t\left[\underline{\underline{\sigma}}\right] \tag{5}$$

with $\underline{\underline{\tau}}_t$ the Reynolds stress tensor, $\underline{\underline{I_3}}$ the identity tensor and $\left[\underline{\underline{\sigma}}\right]$ the mean zero-trace strain rate tensor. In LES, both the Reynolds stress tensor and the mean zero-trace strain rate tensor[3] ($[\underline{\underline{\widetilde{\sigma}}}]$) are known independently, so the relation in eq. (5) can be tested.

The other constitutive relation tested, the QCR, relies also on a tensorial relation:

$$\underline{\underline{\tau}}_t + \frac{2}{3}\langle\rho\rangle[k]\,\underline{\underline{I_3}} = \mu_t\left(\left[\underline{\underline{\sigma}}\right] + c_{QCR}(\left[\underline{\underline{\sigma}}\right]\underline{\underline{O}} - \underline{\underline{O}}\left[\underline{\underline{\sigma}}\right])\right) \tag{6}$$

with $\underline{\underline{O}}$ being the normalised rotation tensor.

The evaluation is carried out in two steps: first the alignment of the left-hand side and the right-hand side tensors is evaluated, then the magnitude are compared.

Alignment criterion

The alignment between the tensors of the Boussinesq constitutive relation is measured using an indicator, as given in eq.(7). The present indicator is similar to that of Schmitt [37], but is able to discriminate aligned and anti-aligned tensors. Two tensors are anti-aligned if they are aligned with opposite

[3]Note that even though $[\underline{\underline{\widetilde{\sigma}}}] = [\underline{\underline{\sigma}}]$, the first notation is kept, in order to distinguish clearly in the equations what comes from LES.

directions. An example of anti-aligned vectors is given in figure 13.

$$\Upsilon = \frac{\underline{\underline{\tau_t^k}} : \left[\underline{\widetilde{\sigma}}\right]}{\left\|\underline{\underline{\tau_t^k}}\right\| \left\| \left[\underline{\widetilde{\sigma}}\right] \right\|} \tag{7}$$

$$\text{with: } \underline{\underline{\tau_t^k}} = -\left\langle \overline{\rho} u_i'' u_j'' \right\rangle + \frac{2}{3} \left\langle \overline{\rho} \right\rangle \left[\widetilde{k}\right] \underline{\underline{I_3}} \tag{8}$$

and $\left[\widetilde{k}\right] = -0.5\tau_{tii} / \left\langle \overline{\rho} \right\rangle$.

Similarly to Schmitt's indicator, when this indicator is equal to 1, the tensors are aligned, and the Boussinesq hypothesis is valid. When this indicator is equal to 0, the tensors are orthogonal, and the Boussinesq hypothesis is invalid. Contrary to Schmitt's indicator, this indicator can be negative. In this case, the tensors are anti-aligned, which means that the Boussinesq constitutive relation would lead to non-physical results. Schmitt suggested that the alignment hypothesis is considered valid as this indicator is greater than 0.86. The same alignment criterion is kept for the present Υ indicator, *i.e.* the alignment hypothesis is considered valid if $\Upsilon \geqslant 0.86$. An illustration is given in figure 13, with vectors in place of tensors.

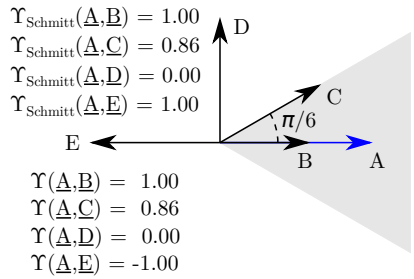

Figure 13: Illustration of the tensor alignment criterion. The grey cone represents the area where the Boussinesq constitutive relation is considered valid.

The alignment indicator is adapted to the QCR as follows:

$$\Upsilon^{QCR} = \frac{\underline{\underline{\tau_t^k}} : \left[\underline{\underline{\sigma^{QCR}}}\right]}{\left\|\underline{\underline{\tau_t^k}}\right\| \left\| \left[\underline{\underline{\sigma^{QCR}}}\right] \right\|} \tag{9}$$

$$\text{with: } \left[\underline{\underline{\sigma^{QCR}}}\right] = \left[\underline{\underline{\widetilde{\sigma}}}\right] + c_{QCR}(\left[\underline{\underline{\widetilde{\sigma}}}\right]\underline{\underline{\widetilde{O}}} - \underline{\underline{\widetilde{O}}}\left[\underline{\underline{\widetilde{\sigma}}}\right]) \tag{10}$$

Magnitude assessment: turbulent viscosity

The second step of the constitutive relation assessment compares the magnitude of the tensors. The turbulent viscosity represents the proportionality coefficient between the Reynolds stress tensor and the constitutive relation tensor (*i.e.* $\left[\underline{\underline{\widetilde{\sigma}}}\right]$ for the Boussinesq constitutive relation and $\left[\underline{\underline{\sigma^{QCR}}}\right]$ for the QCR). Given the LES data available, a first approach is to reconstruct a reference turbulent viscosity as the ratio of the tensor norms:

$$\mu_t^{(0)} = \frac{\left\|\left[\underline{\underline{\tau_t^k}}\right]\right\|}{\left\|\left[\underline{\underline{\widetilde{\sigma}}}\right]\right\|} \; ; \; \mu_t^{(0)QCR} = \frac{\left\|\left[\underline{\underline{\tau_t^k}}\right]\right\|}{\left\|\left[\underline{\underline{\sigma^{QCR}}}\right]\right\|} \tag{11}$$

If the tensors are aligned, *i.e.* $\Upsilon = 1.0$ (resp. $\Upsilon^{QCR} = 1.0$), this value is the turbulent viscosity that verifies the Boussinesq constitutive relation (resp. QCR).

The turbulent viscosity is estimated by the RANS k-ω models as:

$$\mu_t^{(1)} = \langle\overline{\rho}\rangle \frac{\left[\widetilde{k}\right]}{\left[\widetilde{\omega}\right]} \tag{12}$$

The turbulent viscosity μ_t can also be computed from the LES results with $[\widetilde{\omega}] = [\widetilde{\varepsilon}]([\widetilde{k}]C_\mu)^{-1}$, $C_\mu = 0.09$, and $[\widetilde{\varepsilon}]$ derived from the turbulent kinetic energy budget equation as:

$$\langle\overline{\rho}\rangle\,[\widetilde{\varepsilon}] = \underbrace{\left\langle\overline{\tau_{ij}}\frac{\partial u_i''}{\partial x_j}\right\rangle}_{\text{Viscous dissipation}} + \underbrace{\left\langle\overline{\Pi_{ij}}\frac{\partial u_i''}{\partial x_j}\right\rangle}_{\text{SGS dissipation}} \tag{13}$$

4.2. Alignment analysis

The alignment is evaluated by the Υ indicator (resp. Υ^{QCR} indicator), plotted as probability density functions (PDF) and cumulative distribution functions (CDF). Concerning the PDF (for instance, in Fig. 15), there are two sets of bars, a left black bar with a right green bar for each Υ value. A pair of bars

occupies a range of 0.05. The black one (resp. green one) represents the mass weighted percentage of points with Υ (resp. Υ^{QCR}) in the given 0.05 range. The CDF is the integration of the PDF made from -1 upward. Practically, the ordinate corresponding to the abscissa $\Upsilon = 0.86$ (resp. $\Upsilon^{QCR} = 0.86$) represents the mass weighted percentage of points for which the Boussinesq constitutive relation (resp. QCR) is not valid.

The analysis focuses on the regions where turbulence is significant. Only the points whose turbulence intensity (defined as $(2/3[\widetilde{k}]/([\widetilde{u_i}][\widetilde{u_i}]))^{1/2}$) is superior to 5% contribute to the PDF and CDF. This value is chosen so that the corner separation wake and the blade wake are included in the analysis. In order to be grid independent, each point considered is weighted by its mass, calculated as the Jacobian determinant at that point (homogeneous in a control volume) times the density. The analysis focuses first on the entire domain, which includes the inlet domain, the passage domain and the outlet domain, as presented in figure 14. Then, each individual domain is analysed separately.

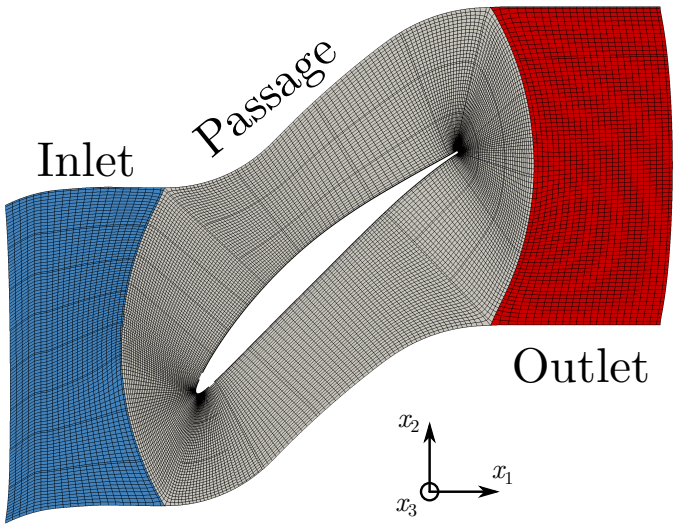

Figure 14: Domains used for the alignment criterion analysis.

The PDF and CDF of the alignment criterion for the entire domain (*i.e.* 100% of the points whose turbulence intensity is superior to 5%) are plotted

in figure 15. Both the Boussinesq constitutive relation and the QCR present points with negative criterion values, indicating negative alignments between the modelled tensor and the actual Reynolds stress tensor. For both constitutive relations, the amount of anti-aligned points remains small, with less than 4% of the points concerned. The PDF of Υ (Boussinesq) increases gradually from 0 to 0.75 and then decreases abruptly, showing that the vast majority of points do not present a correct alignment between the tensors. The peak of the distribution is in the interval $[0.7,\ 0.75]$, below the 0.86 threshold.

In comparison, Υ^{QCR} presents lower densities under 0.75 and more points with higher Υ values, *i.e.* their peaks in the interval $[0.9,\ 0.95]$. The CDF shows the Boussinesq constitutive relation is valid for only 9% of the points, whereas the QCR is valid for 34% of the points. The QCR improves the direction of the tensor.

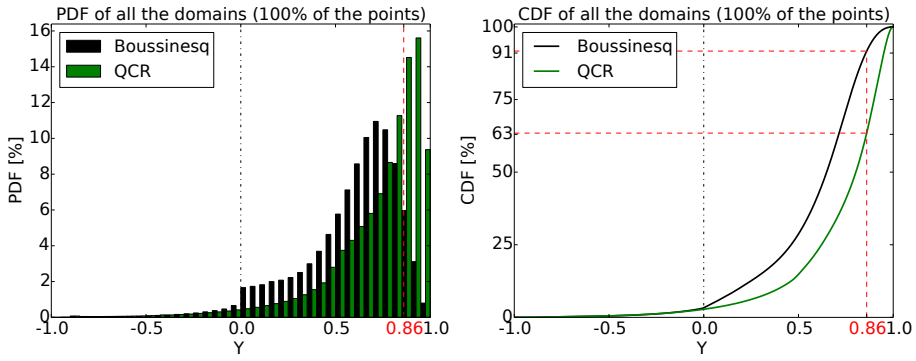

Figure 15: PDF and CDF of the Υ and Υ^{QCR} criteria over the entire domain.

The analysis now focuses separately on the inlet, the passage, and the outlet domains to see if the constitutive relations behave differently for different parts of the flow.

The inlet domain, located upstream of the blades, presents characteristics of a flat-plate turbulent boundary layer. The Boussinesq constitutive relation is expected to present better results on this canonical case. Considering only the points where the turbulence intensity is greater than 5%, the mass-weighted

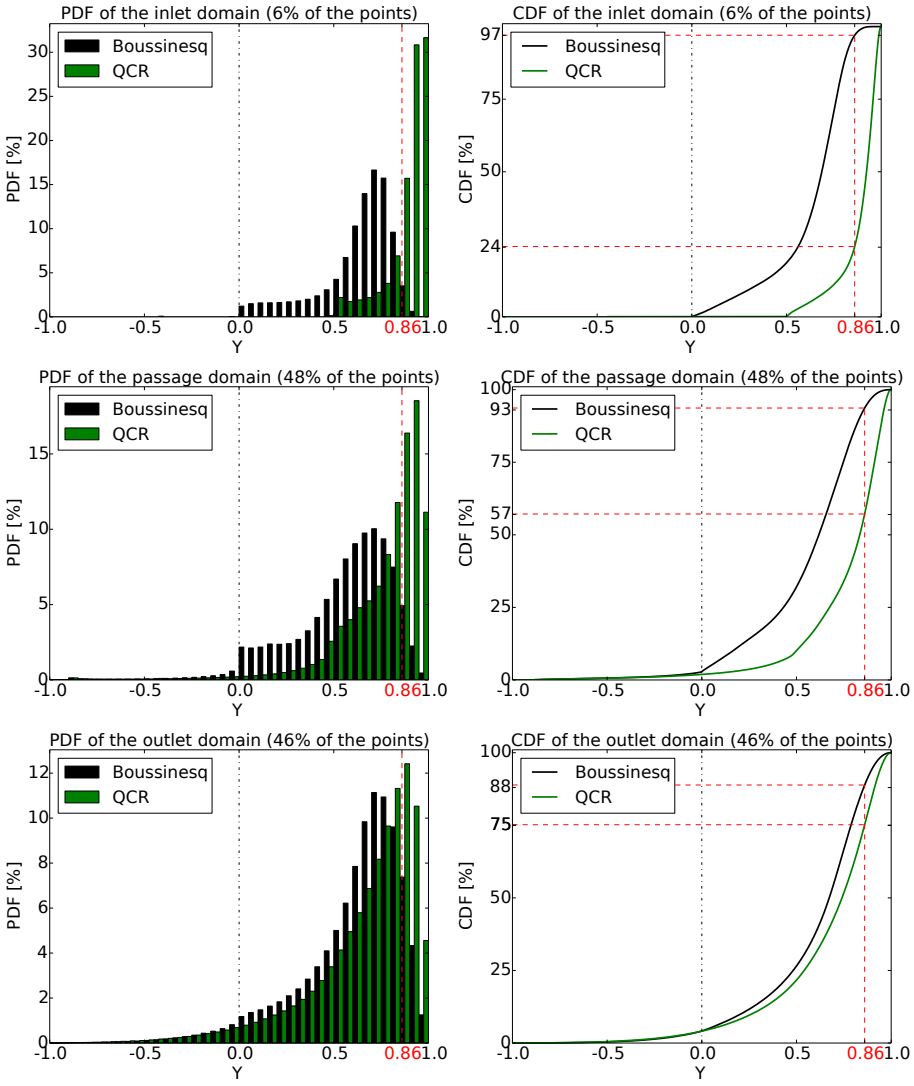

Figure 16: PDF and CDF of the Υ and Υ^{QCR} criteria in the inlet, passage, and outlet domains.

point number of the inlet domain represents 6% of that of the entire domain. The PDF and CDF of the inlet domain are plotted in figure 16. Contrary to expectations, the Boussinesq constitutive relation does not perform better on this canonical flow in the inlet domain. The distribution is similar to the

one of the entire domain, with a peak in the interval [0.7, 0.75], except there is no negative alignment. The CDF shows that the overall alignment is even worse, with 97% of the points invalid for the Boussinesq constitutive relation. In comparison, the QCR presents a significant improvement in this area. The peak of the PDF is in the interval [0.95, 1.0], and the CDF shows that the constitutive relation is valid, in terms of alignment, for 76% of the points. The QCR has an important effect on this canonical flow. This may be partly due to the fact that the coefficient was calibrated in the outer region of a simple boundary layer [13].

The passage domain, located in-between the blades, presents three boundary layers: at the end-wall and on both sides of the blades. The interaction of the end-wall and suction-side boundary layers under adverse pressure gradient forms the corner separation. The flow is three dimensional and vortical, and is more complex than the inlet domain boundary layer. The mass-weighted point number of this domain accounts for 48% of that of the entire domain, considering turbulence intensity greater than 5%. Around 2% of the points are anti-aligned, for both the Boussinesq and the quadratic constitutive relations. The Boussinesq constitutive relation yields similar results to the inlet domain. Inspecting the CDF, the Boussinesq hypothesis is valid for 7% of the points. The QCR yields better results in terms of tensor alignment, but the improvement is limited compared to the inlet domain. The peak of the PDF is inside the area where the alignment hypothesis is valid, but the CDF indicates that the QCR is valid for only 43% of the points.

The last domain is located at the outlet, where the wake of the corner separation develops. The flow is again three-dimensional and highly vortical. The number of points from this domain, weighted by the mass, represents 46% of that of the entire domain. The Boussinesq constitutive relation gives similar results, with slight improvement. Almost all the anti-aligned points of the entire domain are located in the outlet part, in the corner separation wake. Concerning the QCR, the improvement is visible compared to the Boussinesq constitutive relation, but is less significant than for the upstream domains. In

this complex wake region, the QCR behaviour, in terms of tensor alignment, is much closer to the Boussinesq constitutive relation. The CDF shows that the amount of aligned points with QCR is comparable to the Boussinesq results: 25% of aligned points for Υ^{QCR}, close to the value 12% for Υ. This result is counter-intuitive. Given that the formulation of the QCR explicitly contains a normalised rotation tensor, it was expected to be more effective in highly vortical areas.

4.3. Turbulent viscosity comparisons

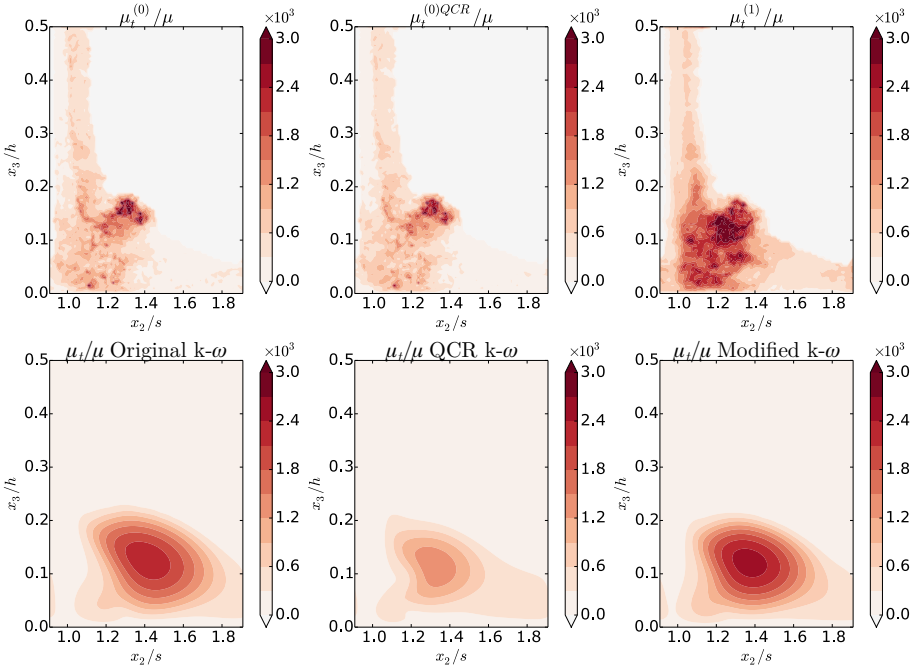

Figure 17: Turbulent viscosities on the 'outlet 1' plane. The *a priori* values from the LES results, defined by eqs. 11 and 12, are presented in the first row. The *a posteriori* values obtained with the RANS simulations are presented in the second row. All the turbulent viscosities (*a priori* and *a posteriori*) are normalised by the reference molecular viscosity μ.

The turbulent viscosities are plotted in figure 17. The LES reference value $\mu_t^{(0)}$ is compared to the LES estimate $\mu_t^{(1)}$ and to the turbulent viscosities obtained directly with the RANS simulations (*a posteriori* values). The turbulent

viscosities are plotted on the 'outlet 1' plane, and normalised by the reference dynamic viscosity $\mu = 1.81 \times 10^{-5}\text{kg.m}^{-1}\text{.s}^{-1}$.

It is first remarkable that the LES turbulent viscosity computed as $\mu_t^{(1)} = \langle\overline{\rho}\rangle\,[\widetilde{k}]/[\widetilde{\omega}]$ is of a comparable order of magnitude as the RANS turbulent viscosities computed as $\mu_t = \langle\rho\rangle\,[k]/[\omega]$, where $[k]$ and $[\omega]$ are provided by the transport equations of the models. As already observed with the Reynolds stresses, RANS simulations are unable to correctly predict the size of the corner separation, where the turbulent viscosity is maximal. The reference turbulent viscosities $\mu_t^{(0)}$ are of the same order of magnitude as the RANS turbulent viscosities μ_t. The similarity between $\mu_t^{(0)}$ and $\mu_t^{(0)QCR}$ values indicates the QCR bears no significant modification on the norm of the constitutive relation tensor. Finally, the $\mu_t^{(1)}$ estimate yields high values inside the corner separation wake (near $x_2/s = 1.1$ and $x_3/h = 0.05$) whereas the reference $\mu_t^{(0)}$ is more concentrated around the separation border ($x_2/s \approx 1.3$ and $x_3/h \approx 0.15$). This is a deficiency of estimating μ_t as $\langle\overline{\rho}\rangle\,[\widetilde{k}]/[\widetilde{\omega}]$.

5. Turbulent kinetic energy budget

The turbulent kinetic energy (TKE) budget, also called turbulence budget, allows to understand the distribution of the TKE terms, between production, dissipation and transport. However, due to the difficulty to measure the combined statistics, it is impossible to directly obtain the TKE budget with the experiment. In this regard, DNS and LES offer an interesting alternative for such an in-depth physical analysis of turbulence.

The LES momentum equation is rearranged to obtain the Reynolds stress budget equation, following the method of Bogey and Bailly [38]. Then the diagonal terms are summed to achieve the following TKE budget formulation:

$$0 = \frac{\partial \langle \overline{\rho} k \rangle}{\partial t} = \underbrace{-\frac{\partial}{\partial x_j}\left(\langle \overline{\rho} k \rangle \left[\widetilde{u_j}\right]\right)}_{\text{Advection}} \underbrace{-\left\langle \overline{\rho} u_i'' u_j'' \right\rangle \frac{\partial \left[\widetilde{u_i}\right]}{\partial x_j}}_{\text{Production}} \underbrace{-\frac{\partial \left\langle \overline{\rho} k u_j'' \right\rangle}{\partial x_j}}_{\text{Turbulent diffusion}}$$
$$\underbrace{-\frac{\partial \langle u_i'' p' \rangle}{\partial x_i}}_{\text{Pressure Diffusion}} \underbrace{+\left\langle p' \frac{\partial u_i''}{\partial x_i} \right\rangle}_{\text{Pressure dilatation}} \underbrace{-\langle u_i'' \rangle \frac{\partial \langle \overline{p} \rangle}{\partial x_i}}_{\substack{\text{Fluctuating velocity-} \\ \text{pressure gradient correlation}}}$$
$$\underbrace{+\frac{\partial \langle \overline{\tau_{ij}} u_i'' \rangle}{\partial x_j}}_{\text{Viscous diffusion}} \underbrace{-\left\langle \overline{\tau_{ij}} \frac{\partial u_i''}{\partial x_j} \right\rangle}_{\text{Viscous dissipation}} \underbrace{+\frac{\partial \left\langle \overline{\Pi_{ij}} u_i'' \right\rangle}{\partial x_j}}_{\text{SGS diffusion}} \underbrace{-\left\langle \overline{\Pi_{ij}} \frac{\partial u_i''}{\partial x_j} \right\rangle}_{\text{SGS dissipation}} \underbrace{+\Xi}_{\text{Numerical residual}} \tag{14}$$

with $\underline{\underline{\Pi}}$ the sub-grid scale stress tensor [28] and Ξ the numerical residual term, computed as the opposite value of the sum of all the other terms.

In RANS with a $k-\omega$ model, the TKE budget is modelled by the k equation [34]. The Wilcox $k-\omega$ model is known to over-predict k production where anisotropy is important [39]. Consequently, a k-production limiter [40] is implemented in the solver, in the form of a clipping of the k-production term, when the k-production term is superior to ten times the k-dissipation term. This limiter does not usually appear in the k equation, but it is explicitly introduced in the budget, as a dissipative term Λ. Moreover, the k equation being directly solved in RANS, the sum of all the other terms except the production limiter is negligible. Thus, the numerical residual represents directly the opposite of the production limiter.

$$\frac{\partial \langle \rho \rangle [k]}{\partial t} = \underbrace{\tau_{t,ij} \frac{\partial [u_i]}{\partial x_j}}_{\text{Production}} \underbrace{-\frac{\partial \langle \rho \rangle [k] [u_j]}{\partial x_j}}_{\text{Advection}} \underbrace{+\frac{\partial}{\partial x_j}\left(\mu \frac{\partial [k]}{\partial x_j}\right)}_{\substack{\text{Molecular} \\ \text{diffusion}}} \underbrace{+\frac{\partial}{\partial x_j}\left(\frac{\mu_t}{\sigma_k} \frac{\partial [k]}{\partial x_j}\right)}_{\substack{\text{Turbulent transport \&} \\ \text{pressure diffusion}}}$$
$$\underbrace{-c_k \langle \rho \rangle [k] [\omega]}_{\text{Dissipation}} \underbrace{+\Lambda}_{\substack{k \text{ production} \\ \text{limiter}}} \underbrace{+\Xi}_{\substack{\text{Numerical} \\ \text{residual}}} \tag{15}$$

Note that $\tau_{t,ij}$ is computed with either the Boussinesq constitutive relation (for the original and modified $k-\omega$ models) or the QCR (for the QCR $k-\omega$ model).

5.1. Validation on a flat plate case

The implementation of the budget extraction for LES is validated on a flat-plate boundary layer simulation, against DNS results from Jiménez *et al.*[21]. The characteristics of flow, mesh and numerical schemes are chosen as similar as possible to those of the corner separation case, and the simulations are realised with the same solver. The boundary-layer is described up to $\mathrm{Re}_x = 1.3 \times 10^6$, with a source term to trip transition at $\mathrm{Re}_x = 3.0 \times 10^5$. The details of the trip implementation are presented by Boudet *et al.*[31]. The position of the trip is indicated in figure 18 by a triangle. Because the solver uses a compressible formulation, the Mach number is chosen small enough to limit compressible effects but high enough to improve convergence speed, *i.e.* $M = 0.2$, which yields a free-stream velocity $u_e = 70\mathrm{m.s}^{-1}$. The air density is $\rho_e = 1.117\mathrm{kg.m}^{-3}$ and the dynamic viscosity is $\mu = 1.81 \times 10^{-5}\mathrm{kg.m}^{-1}.\mathrm{s}^{-1}$. The length of the computational domain in the stream-wise direction is $L_{x_1} = 0.3\mathrm{m}$. To simulate properly the boundary-layer at the outlet, the computational domain height is set to twice the estimated boundary-layer thickness, $L_{x_2} = 0.0117\mathrm{m}$. The span-wise width corresponds to the estimated boundary-layer thickness at the outlet, $L_{x_3} = 0.00586\mathrm{m}$. The mesh is uniform in the stream-wise and span-wise directions. In the wall-normal direction, the point distribution follows a geometrical law with an expansion ratio of 1.10. The non-dimensional cell sizes at the wall, in wall units, are $\Delta x_1^+ \leqslant 60$, $\Delta x_2^+ \leqslant 2$ and $\Delta x_3^+ \leqslant 30$. This refinement level is classical in wall resolved LES. The computational domain is made of $1035 \times 60 \times 44 = 2\,732\,400$ points. At the inlet, the velocity vector and density are imposed. The outlet boundary and upper boundary are set to a mixed pressure outlet, which combines atmospheric static pressure prescription ($p = 101\,340\mathrm{Pa}$) and a non-reflection condition. It allows pressure waves to exit the computational domain. The wall boundary condition is set to no-slip adiabatic. The lateral boundary conditions are set to periodic. The spatial scheme for the inviscid fluxes is a 4-point Jameson centred scheme, with a fourth-order artificial viscosity (coefficient: 0.002, see [31] for its definition). A 2-point centred scheme is used for the viscous fluxes. The temporal discretisation uses

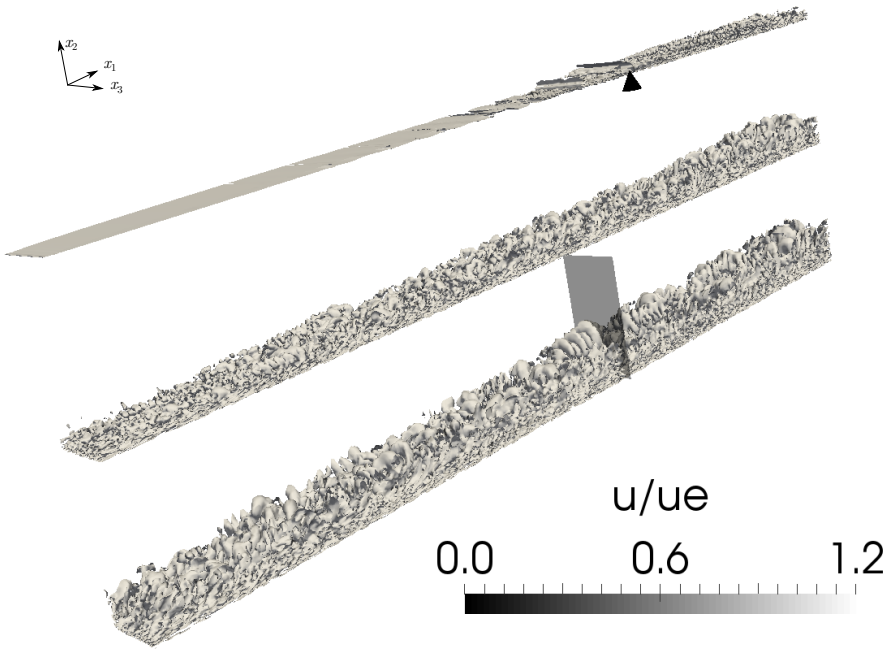

Figure 18: Flat-plate boundary-layer test-case for the validation of the LES TKE-budget implementation: instantaneous iso-surface of Q-criterion, coloured by normalised stream-wise velocity. For visualisation, the total length is cut into three pieces, which are piled from top to bottom. The triangle marks the trip abscissa, and the grey plane the extraction abscissa for the TKE budget.

a three-step Runge-Kutta scheme, with a global constant time step of 10^{-8}s, corresponding to CFL = 0.95 (based on the inflow velocity, the speed of sound, and the minimal grid size). The simulation is carried out with the SISM SGS model [33]. The exponential average used to extract the mean flow for the SISM [41] is calibrated with a frequency of $13,340$Hz. This value corresponds to the ratio between a characteristic velocity (the stream-wise friction velocity at the transition point) and a characteristic length (the boundary-layer displacement thickness at the transition point).

The TKE budget is extracted at a constant x_1 position where $\mathrm{Re}_{\delta_2} = 1968$, with δ_2 the momentum thickness. The sampling period is $10^{-2}\mu$s (= LES time step). The total duration of 12.0ms is used for the calculation of the statistics.

Some of the TKE budget terms, presented in equation (14), are grouped for the presentation. The advection and production terms are kept separate. The viscous and SGS dissipations are summed into a dissipation term. The viscous diffusion and SGS diffusion are summed into a viscous diffusion term. The remainders are summed into a single term, representing the pressure dilatation and turbulent diffusion. The numerical residual is computed as the opposite of the sum of all budget terms. The budget terms are normalised by $(\rho_e^2 u_e^2)/\mu$.

The budget evolution is analysed against the sample time used for its calculation, to check its convergence. For a given sample time, a term is calculated by the integral of its absolute value over the height, and divided by the production term computed with the maximal sample time.

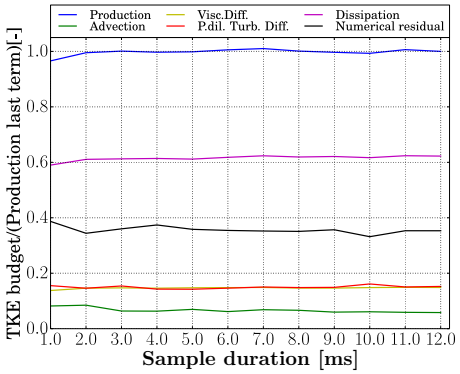

Figure 19: TKE budget terms against duration time. The terms are normalised by the production term computed with the maximal sample duration.

Figure 19 shows the budget evolution terms remains unchanged with sample time, indicating the statistical convergence is satisfactory. However, a non null numerical residual is observed. This term is stationary, indicating that the numerical residual is not due to an insufficient statistical convergence, but a stationary numerical dissipation.

The budget computed over the maximal sample duration is compared to the DNS results from Jimenez *et al.*[21]. The results are presented on the left subplot of figure 20. The comparison with DNS shows that the LES is able to describe

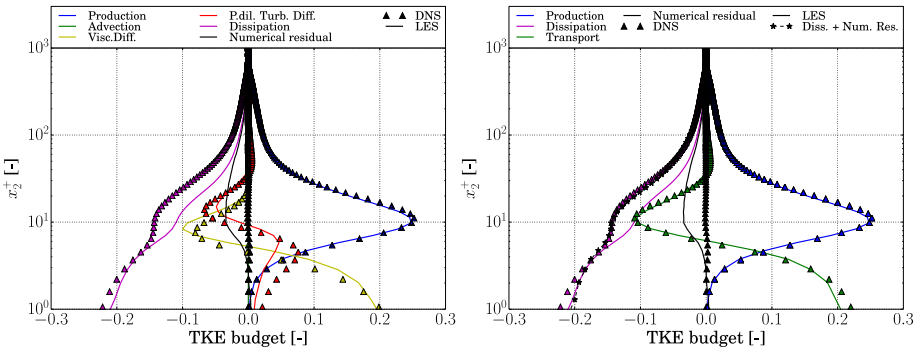

Figure 20: TKE budget in a flat-plate boundary layer, extracted at $\mathrm{Re}_{\delta_2} = 1968$. Left : the terms are presented separately. Right : the pressure dilatation and turbulent diffusion term, the advection term and the viscous diffusion term are grouped into a single transport term.

the TKE budget. The production and transport terms of the LES are very close to the DNS, and the difference on the dissipation term remains moderate. The viscous diffusion term is slightly over estimated, whereas the pressure dilatation and turbulent diffusion term is slightly underestimated. The numerical residual is negative, thus acting as a numerical dissipation. The numerical dissipation is maximal at $x_2^+ \approx 10$, but remains smaller than the other terms.

In order to summarise the physical meaning of the terms, the pressure dilatation and turbulent diffusion term, the advection term and the viscous diffusion term are grouped into a single transport term. The results are presented on the right subplot of figure 20. The sum of the dissipation term and the numerical residual term is also plotted. The transport term presents very good agreement with the DNS. This means that the transport mechanisms of the TKE is appropriately predicted. When the dissipation and the numerical dissipation are summed, the resulting term is very close to the DNS dissipation term. The numerical residual represents various numerical effects that are not taken into account by the viscous and SGS dissipation. Among these effects, we can cite the effects of the numerical schemes, the effects of the mesh, or the effects of the computational method (finite difference) used to compute the TKE budget. These effects arise partly because the TKE budget equation is not directly

solved, but reconstructed. Consequently, non-conservative effects can develop. Finally, the LES gives excellent results close to the wall ($x_2^+ \leqslant 3$), where the three physical terms agree well with the DNS.

Although the LES results present more numerical dissipation than the DNS, the prediction of the different terms is considered correct enough to be exploited for a physical analysis. This behaviour is common for LES TKE budget extraction. For example, a similar amount of numerical dissipation can be found in the work of Schiavo *et al.*[42].

5.2. Application to the corner separation case

The TKE budget terms are extracted on the 'outlet 1' plane. In order to facilitate the comparison, the terms are grouped by their physical meaning, as done during the flat-plate validation: the production term and the numerical residual term are left isolated, while the dissipation is the sum of the viscous and SGS dissipations and the transport is the sum of the remaining terms (among which the SGS diffusion). Thus, the SGS terms are included in the group terms that are plotted. For the RANS simulations, the numerical residual presents directly the opposite of the production limiter. The numerical residual is presented first, in order to gauge the quality of the budget extraction.

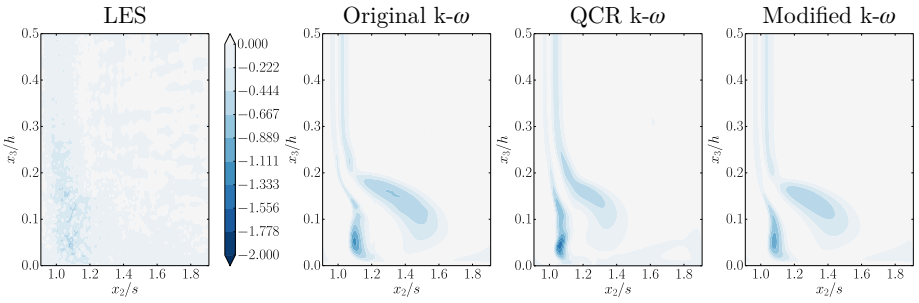

Figure 21: Numerical residual of the TKE budget on the 'outlet 1' plane, normalised by $(\rho_e^2 u_e^4)/\mu$.

The numerical residual term on the 'outlet 1' plane is presented in figure 21. It is negative, thus corresponding to a dissipative effect. For the LES, this term

is not negligible compared to the other budget terms (in Figs 22, 23 and 24) but remains moderate. Its amplitude is smaller than a quarter of the amplitude of the production and dissipation, thus its impact on the budget does not modify the physical analysis.

The three RANS simulations show a significant numerical residual corresponding to the activation of the k-production limiter, which clips the production if it is more than ten times the dissipation. This behaviour is expected, given that the limitation is to occur in areas of high anisotropy. The three RANS simulations show a similar activation of the k-production limiter, inside the wake of the corner separation, where the flow is highly vortical.

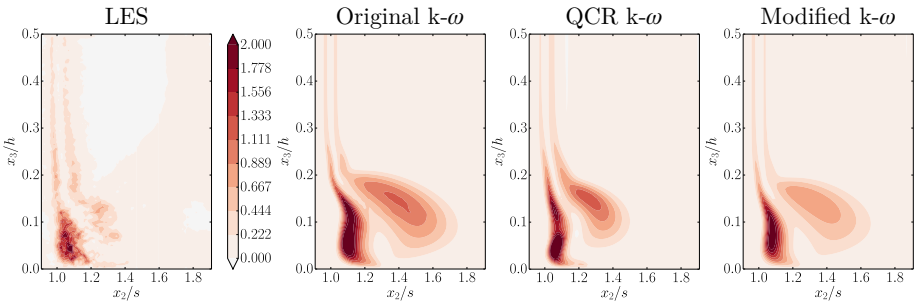

Figure 22: TKE production on the 'outlet 1' plane, normalised by $(\rho_e^2 u_e^4)/\mu$.

The production term at 'outlet 1' is shown in figure 22. The LES shows two distinct lobes. The first lobe, centred around $x_2/s = 1.1$ and $x_3/h = 0.05$, is the main area of production. A second lobe of lower intensity is found around $x_2/s = 1.3$ and $x_3/h = 0.1$. These two areas are inside the area of maximal Reynolds stresses and maximal losses, as shown in figures 10, 11 and 12.

The RANS results present a similar topology to the LES result, *i.e.* two lobes are well delimited. However, all the RANS simulations over-predict the size of the lobes and the intensity of the term. The over-prediction is remarkable for the external lobe (at $x_2/s \simeq 1.3$ and $x_3/h \simeq 0.15$). The QCR $k-\omega$ model reduces the intensity of the production term and the lobe extent, and so does, but less efficiently, the modified $k-\omega$ model. The QCR $k-\omega$ model shows the best comparison to the LES.

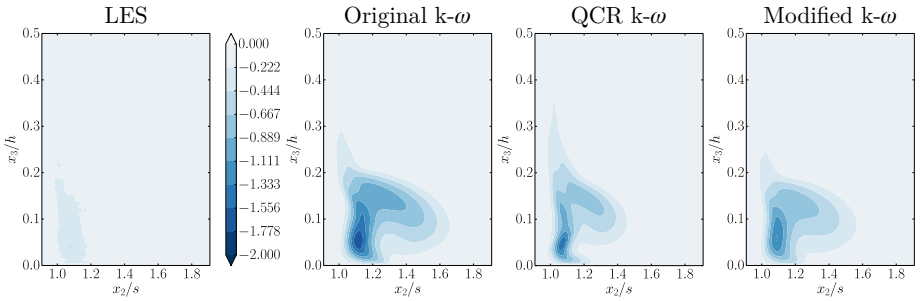

Figure 23: TKE dissipation on the 'outlet 1' plane, normalised by $(\rho_e^2 u_e^4)/\mu$.

The dissipation term at the section 'outlet 1' is given in figure 23. The LES dissipation in the wake is very weak. The behaviour of the RANS simulations is very different. For the three RANS simulations, the dissipation in the wake is intense and superimposed with the area of production. The original $k-\omega$ model shows a notable overestimation of the dissipation. The intensity is reduced by the QCR and modified $k-\omega$ models. But the reduction is limited in comparison to the LES. As for the production term, the QCR $k-\omega$ model gives the best description of the physics.

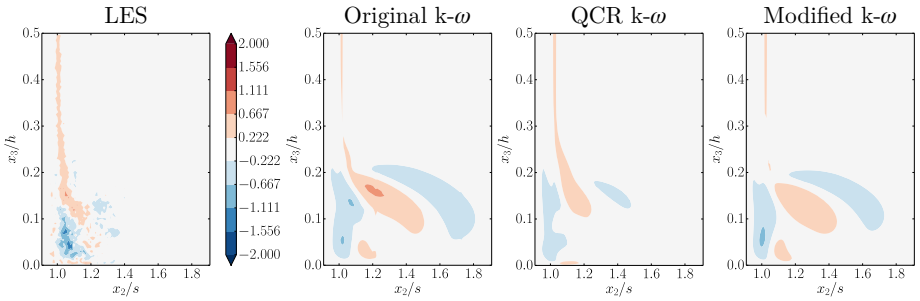

Figure 24: TKE transport on the 'outlet 1' plane, normalised by $(\rho_e^2 u_e^4)/\mu$.

Figure 24 presents the transport term at 'outlet 1'. The LES transport develops in the blade and corner separation wakes. The TKE is taken from areas of production to be transported to dissipative places, close to the walls and downstream. With regard to RANS, the amplitude of the transport term is moderate compared with the production or dissipation terms. This is the

counterpoint of the non-physical behaviour of the RANS models. Turbulent kinetic energy is dissipated where it is produced, and not transported. However, given the overestimation of production and dissipation, transport shows intensities comparable with the LES. A particularly good estimate of the intensity is achieved by the original $k-\omega$ model. The QCR $k-\omega$ model gives a better estimate in terms of size of the maximal transport area. The modified model does not show such a strong improvement.

6. Conclusion

The main objective of the present work was to characterise in detail the behaviour of classic RANS models in a corner separation flow. The characterisation has been made through various aspects, from the analysis of the Reynolds stress tensor to the term-to-term comparison of the modelled TKE budget equation, using LES results as reference.

The three RANS models fail to accurately predict the Reynolds stresses. Both the topology and intensity are wrongly estimated. Among the three models, the QCR $k-\omega$ model gives the best agreement with the LES. The incorrect estimation of the Reynolds stresses can be a consequence of a defect of the constitutive relation, a defect of the modelled turbulence equations, or a coupling of the two.

The alignment hypothesis between the Reynolds stresses and the velocity gradient tensor is generally not valid. The Boussinesq constitutive relation relies on an alignment that is not valid even on canonical flows, such as a developing boundary layer. The quadratic constitutive relation, which accounts for the local vorticity of the flow, gives much better results in the inlet and corner separation domain. Its improvement to the corner separation wake domain is, however, limited. Concerning the estimate of the eddy-viscosity, the use of k and ω gives fairly good results.

The modelled TKE budget (k equation) presents almost the same behaviour for the three RANS turbulence models. The production term is not accurately

predicted, which is directly associated with the erroneous representation of the Reynolds stresses. The transport term is weak compared to the other terms in the RANS simulations, while it is not negligible in the LES. The dissipation term is locally opposite to the production term in the RANS simulations, while the LES TKE dissipation is not located in the same areas as the production. This superimposition is typical of the RANS turbulence models that rely implicitly on the strong hypothesis of equilibrium turbulence, *i.e.* a local equilibrium between production and dissipation with little transport.

Nomenclature

c	Blade chord length [m]
c_a	Chord length projection in the x_1 direction [m]
c_{QCR}	Constant of the quadratic constitutive relation
Cp	Mean static-pressure coefficient
Cp_t	Mean total-pressure loss coefficient
C_μ	Turbulence model constant
fr_1	Factor in the modified $k-\omega$ model
h	Blade span [m]
k	Turbulent kinetic energy [$m^{-2}.s^{-2}$]
L_{x_1}	Length of the flat-plate domain [m]
L_{x_2}	Height of the flat-plate domain [m]
L_{x_3}	Width of the flat-plate domain [m]
M	Mach number
$\underline{\underline{O}}$	Normalised rotation tensor
p	Local mean static pressure [Pa]
p_e	Inflow (reference) mean static-pressure [Pa]
p_t	Local mean total-pressure [Pa]
p_{te}	Inflow (reference) mean total pressure [Pa]
Re_c	Chord based Reynolds number
Re_{δ_2}	Momentum thickness based Reynolds number

Re_x	Stream-wise Reynolds number
s	Pitch [m]
S	Modulus of the mean strain-rate tensor [s^{-1}]
$\underline{u}$	Local velocity vector [$m.s^{-1}$]
u_e	Free-stream (reference) velocity [$m.s^{-1}$]
x_1	Stream-wise direction
x_2	Pitch-wise direction
x_3	Span-wise direction
γ	Blade stagger angle [°]
δ	Boundary-layer thickness [m]
δ_2	Boundary-layer momentum thickness [m]
Δy^+	Non-dimensional wall distance
ϵ	Turbulence dissipation rate [$m^{-2}.s^{-3}$]
Λ	k-production limiter [$kg.m^{-1}.s^{-3}$]
μ	Dynamic viscosity [$kg.m^{-1}.s^{-1}$]
μ_{SGS}	Sub-grid scale viscosity [$kg.m^{-1}.s^{-1}$]
μ_t	Eddy-viscosity [$kg.m^{-1}.s^{-1}$]
$\mu_t^{(0)}$	LES-based reference turbulent viscosity assuming the Boussinesq constitutive relation is valid [$kg.m^{-1}.s^{-1}$]
$\mu_t^{(0)QCR}$	LES-based reference turbulent viscosity assuming the QCR is valid [$kg.m^{-1}.s^{-1}$]
$\mu_t^{(1)}$	LES-based estimate of the turbulent viscosity [$kg.m^{-1}.s^{-1}$]
Ξ	Numerical residual [$kg.m^{-1}.s^{-3}$]
Π	SGS stress tensor [$kg.m^{-1}.s^{-2}$]
ρ	Local density [$kg.m^{-3}$]
ρ_e	Reference density [$kg.m^{-3}$]
$\underline{\underline{\sigma}}$	Mean zero-trace strain rate tensor [s^{-1}]
$\underline{\underline{\tau}}$	Viscous stress tensor [$kg.m^{-1}.s^{-2}$]
$\underline{\underline{\tau_t}}$	Reynolds stress tensor [$kg.m^{-1}.s^{-2}$]
Υ	Alignment indicator for the Boussinesq constitutive relation

Υ^{QCR}	Alignment indicator for the QCR
ω	Specific turbulence dissipation rate [s^{-1}]
Ω	Modulus of the mean rotation tensor [s^{-1}]

Acknowledgements

This study was supported by the Franco-Chinese project VortexFlowCFD, co-funded by Safran Aircraft Engines and the French National Research and Technology Agency (ANRT). The simulations were performed using HPC resources from GENCI-CINES (Grant c2015-2a5039).

References

References

[1] P. Tucker, Unsteady computational fluid dynamics in aeronautics, Vol. 104, Springer Science & Business Media, 2013.

[2] A. M. Yocum, W. F. O'Brien, Separated flow in a low-speed two-dimensional cascade: part I-flow visualization and time-mean velocity measurements, Journal of Turbomachinery 115 (1993) 409–420.

[3] A. M. Yocum, W. F. O'Brien, Separated flow in a low-speed two-dimensional cascade: part II-cascade performance, Journal of Turbomachinery 115 (1993) 421–434.

[4] S. A. Gbadebo, T. P. Hynes, N. A. Cumpsty, Influence of surface roughness on three-dimensional separation in axial compressors, Journal of Turbomachinery 115 (4) (2004) 455–463.

[5] S. A. Gbadebo, N. A. Cumpsty, T. P. Hynes, Three-dimensional separations in axial compressors, Journal of Turbomachinery 127 (2) (2005) 331.

[6] S. A. Gbadebo, N. A. Cumpsty, T. P. Hynes, Interaction of tip clearance flow and three-dimensional separations in axial compressors, Journal of Turbomachinery 129 (4) (2007) 679.

[7] W. Ma, X. Ottavy, L. Lu, F. Leboeuf, Intermittent corner separation in a linear compressor cascade, Experiments in Fluids 54 (6) (2013) 1–17.

[8] C. Hah, J. Loellbach, Development of hub corner stall and its influence on the performance of axial compressor blade rows, Journal of turbomachinery 121 (1) (1999) 67–77.

[9] Y. Liu, L. Lu, L. Fang, F. Gao, Modification of Spalart-Allmaras model with consideration of turbulence energy backscatter using velocity helicity, Physics Letters A 375 (24) (2011) 2377–2381.

[10] Y. Liu, H. Yan, L. Fang, L. Lu, Q. Li, L. Shao, Modified k-ω model using kinematic vorticity for corner separation in compressor cascades, Science China Technological Sciences (Jan. 2016).

[11] F. Gao, W. Ma, G. Zambonini, J. Boudet, X. Ottavy, L. Lu, L. Shao, Large-eddy simulation of 3-D corner separation in a linear compressor cascade, Physics of Fluids 27 (8) (2015) 085105.

[12] M. Bordji, F. Gand, S. Deck, V. Brunet, Investigation of a nonlinear Reynolds-averaged Navier-Stokes closure for corner flows, AIAA Journal (2015) 1–13.

[13] P. R. Spalart, Strategies for turbulence modelling and simulations, International Journal of Heat and Fluid Flow 21 (3) (2000) 252–263.

[14] X. Su, X. Yuan, Improved compressor corner separation prediction using the quadratic constitutive relation, Proceedings of the Institution of Mechanical Engineers, Part A: Journal of Power and Energy 231 (7) (2017) 618–630.

[15] P. Spalart, S. R. Allmaras, A one-equation turbulence model for aerodynamic flows, La Recherche Aérospatiale (No. 1) (1994) 5 – 21.

[16] P. Sagaut, Large Eddy Simulation for Incompressible Flows: An Introduction, Springer Science & Business Media, 2006.

[17] D. You, M. Wang, P. Moin, R. Mittal, Large-eddy simulation analysis of mechanisms for viscous losses in a turbomachinery tip-clearance flow, Journal of Fluid Mechanics 586 (2007) 177.

[18] J. Boudet, A. Cahuzac, P. Kausche, M. C. Jacob, Zonal large-eddy simulation of a fan tip-clearance flow, with evidence of vortex wandering, Journal of Turbomachinery 137 (6) (2015) 061001.

[19] F. Gao, Advanced numerical simulation of corner separation in a linear compressor cascade, PhD Thesis, École Centrale de Lyon, Ecully (2014).

[20] F. Gao, G. Zambonini, J. Boudet, X. Ottavy, L. Lu, L. Shao, Unsteady behavior of corner separation in a compressor cascade: Large eddy simulation and experimental study, Proceedings of the Institution of Mechanical Engineers, Part A: Journal of Power and Energy 229 (5) (2015) 508–519.

[21] J. Jiménez, S. Hoyas, M. P. Simens, Y. Mizuno, Turbulent boundary layers and channels at moderate Reynolds numbers, Journal of Fluid Mechanics 657 (2010) 335–360.

[22] W. Ma, Experimental investigation of corner stall in a linear compressor cascade, PhD Thesis, École Centrale de Lyon, Ecully (2012).

[23] W. Ma, X. Ottavy, L. Lu, F. Leboeuf, F. Gao, Experimental Study of Corner Stall in a Linear Compressor Cascade, Chinese Journal of Aeronautics 24 (3) (2011) 235–242.

[24] G. Zambonini, X. Ottavy, J. Kriegseis, Corner separation dynamics in a linear compressor cascade, Journal of Fluids Engineering 139 (6) (2017) 061101.

[25] G. Zambonini, X. Ottavy, Unsteady pressure investigations of corner separated flow in a linear compressor cascade, in: Proceedings of the ASME Turbo Expo 2015: Turbine Technical Conference and Exposition, paper GT2015-42073.

[26] G. Zambonini, Unsteady dynamics of corner separation in a linear compressor cascade, PhD Thesis, École Centrale de Lyon, Ecully (Dec. 2016).

[27] F. Gao, W. Ma, J. Sun, J. Boudet, X. Ottavy, Y. Liu, L. Lu, L. Shao, Parameter study on numerical simulation of corner separation in LMFA-NACA65 linear compressor cascade, Chinese Journal of Aeronautics 30 (1) (2017) 15–30.

[28] J. Boudet, J. Caro, L. Shao, E. Lévêque, Numerical studies towards practical large-eddy simulation, Journal of Thermal Science 16 (4) (2007) 328–336.

[29] C. Bogey, C. Bailly, Three-dimensional non-reflective boundary conditions for acoustic simulations: far field formulation and validation test cases, Acta Acustica united with Acustica 88 (4) (2002) 463–471.

[30] A. Jameson, W. Schmidt, E. Turkel, Numerical solutions of the Euler equations by finite volume methods using Runge-Kutta time-stepping schemes, AIAA paper 1259 (1981) 1981.

[31] J. Boudet, J. F. Monier, F. Gao, Implementation of a roughness element to trip transition in large-eddy simulation, Journal of Thermal Science 24 (1) (2015) 30–36.

[32] J. M. Weiss, W. A. Smith, Preconditioning applied to variable and constant density flows, AIAA Journal 33 (11) (1995) 2050–2057.

[33] E. Lévêque, F. Toschi, L. Shao, J.-P. Bertoglio, Shear-improved Smagorinsky model for large-eddy simulation of wall-bounded turbulent flows, Journal of Fluid Mechanics 570 (2007) 491.

[34] D. Wilcox, C., Reassessment of the scale-determining equation for advanced turbulence models, AIAA Journal 26 (11) (1988) 1299 – 1310.

[35] J. D. Denton, Some limitations of turbomachinery CFD, in: paper GT2010-22540, ASME, 2010, pp. 735–745.

[36] A. Favre, Problems of hydrodynamics and continuum mechanics, Society for Industrial and Applied Mathematics, Philadelphia (1969) 231.

[37] F. G. Schmitt, About Boussinesq's turbulent viscosity hypothesis: historical remarks and a direct evaluation of its validity, Comptes Rendus Mécanique 335 (9-10) (2007) 617–627.

[38] C. Bogey, C. Bailly, Turbulence and energy budget in a self-preserving round jet: direct evaluation using large eddy simulation, Journal of Fluid Mechanics 627 (2009) 129–160.

[39] W. C. Strahle, Stagnation point flows with freestream turbulence - The matching condition, AIAA Journal 23 (11) (1985) 1822–1824.

[40] F. R. Menter, Two-equation eddy-viscosity turbulence models for engineering applications, AIAA Journal 32 (8) (1994) 1598–1605.

[41] A. Cahuzac, J. Boudet, P. Borgnat, E. Lévêque, Smoothing algorithms for mean-flow extraction in large-eddy simulation of complex turbulent flows, Physics of Fluids 22 (12) (2010) 125104.

[42] L. A. C. A. Schiavo, W. R. Wolf, J. L. F. Azevedo, Turbulent kinetic energy budgets in wall bounded flows with pressure gradients and separation, Physics of Fluids 29 (11) (2017) 115108–1 – 115108–15.